



OPEN

High gain/bandwidth off-chip antenna loaded with metamaterial unit-cell impedance matching circuit for sub-terahertz near-field electronic systems

Mohammad Alibakhshikenari^{1✉}, Bal S. Virdee², Dion Mariyanayagam², Valeria Vadalà³, Mohammad Naser-Moghadas⁴, Chan H. See⁵, Iyad Dayoub⁶, Sonia Aïssa⁷, Patrizia Livreri⁸, Shah Nawaz Burokur⁹, Anna Pietrenko-Dabrowska¹⁰, Francisco Falcone^{11,12}, Slawomir Koziel^{13,10} & Ernesto Limiti¹⁴

An innovative off-chip antenna (OCA) is presented that exhibits high gain and efficiency performance at the terahertz (THz) band and has a wide operational bandwidth. The proposed OCA is implemented on stacked silicon layers and consists of an open circuit meandering line. It is shown that by loading the antenna with an array of subwavelength circular dielectric slots and terminating it with a metamaterial unit cell, its impedance bandwidth is enhanced by a factor of two and its gain on average by about 4 dB. Unlike conventional antennas, where the energy is dissipated in a resistive load, the technique proposed here significantly reduces losses. The antenna is excited from underneath the antenna by coupling RF energy from an open-circuited feedline through a slot in the ground-plane of the middle substrate layer. The feedline is shielded with another substrate layer which has a ground-plane on its opposite surface to mitigate the influence of the structure on which the antenna is mounted. The antenna has the dimensions $12.3 \times 4.5 \times 0.905 \text{ mm}^3$ and operates across the 0.137–0.158 THz band corresponding to a fractional bandwidth of 14.23%. Over this frequency range the average measured gain and efficiency are 8.6 dBi and 77%, respectively. These characteristics makes the proposed antenna suitable for integration in sub-terahertz near-field electronic systems such as radio frequency identification (RFID) devices with high spatial resolution.

Terahertz (THz) technologies have lately attracted enormous interest in the research and commercial sectors for various applications such as noninvasive biomedical imaging¹, detection of defects², and short-range wireless communications³. The shorter THz wavelength, compared to that of microwave and millimeter waves, provides high spatial resolution, which is essential for biomedical imaging and defect detection. Moreover, the very large

¹Department of Signal Theory and Communications, Universidad Carlos III de Madrid, 28911 Leganés, Madrid, Spain. ²Center for Communications Technology, London Metropolitan University, London N7 8DB, UK. ³Department of Physic, Milan-Bicocca University, Milan, Italy. ⁴Department of Electrical and Computer Engineering, Science and Research Branch, Islamic Azad University, Tehran 14778-93855, Iran. ⁵School of Engineering and the Built Environment, Edinburgh Napier University, 10 Colinton Rd., Edinburgh EH10 5DT, UK. ⁶Université Polytechnique Hauts-de-France, CNRS, University of Lille, ISEN, Institut d'électronique de Microélectronique et de Nanotechnologie, and INSA Des Hauts de France, Valenciennes, France. ⁷Institut National de la Recherche Scientifique (INRS), University of Québec, Montréal, QC H5A 1K6, Canada. ⁸Department of Engineering, University of Palermo, Viale delle Scienze BLDG 9, 90128 Palermo, Italy. ⁹LEME, UPL, Univ Paris Nanterre, 92410 Ville d'Avray, France. ¹⁰Faculty of Electronics, Telecommunications and Informatics, Gdansk University of Technology, 80-233 Gdansk, Poland. ¹¹Department of Electric, Electronic and Communication Engineering and the Institute of Smart Cities, Public University of Navarre, 31006 Pamplona, Spain. ¹²School of Engineering and Sciences, Tecnológico de Monterrey, 64849 Monterrey, Mexico. ¹³Engineering Optimization and Modeling Center, Reykjavik University, 101 Reykjavik, Iceland. ¹⁴Electronic Engineering Department, University of Rome "Tor Vergata", Via Del Politecnico 1, 00133 Rome, Italy. ✉email: mohammad.alibakhshikenari@uc3m.es

bandwidth available at the THz-band (0.1–1 THz) overcomes current issues of data rate and capacity limitations in wireless systems.

Existing THz technologies are bulky and expensive, which makes them unattractive for portable devices⁴. However, it is now possible to implement highly integrated THz systems on a chip using silicon-based CMOS process, which offers great advantages in terms of cost and ease of fabrication compared with compound semiconductors (e.g., III–V semiconductors). The critical component of any wireless system is the antenna because it interfaces the system to the propagating medium and is responsible for signal transmission and reception. The size of the antenna is related to the wavelength of operation. At THz band the shorter wavelength makes possible the development of miniature antennas suitable for integrating with the THz chip. However, implementation of the miniature antennas requires consideration of unwanted parasitic effects that can undermine the system performance, and the uncertainty introduced by wire or flip-chip bonding⁵, as the antenna is directly connected to the integrated circuit.

Maximum range of THz systems and how much power they can receive/capture depends on the gain of the antenna which in turn determines the equivalent isotropic radiated power (EIRP). The gain and radiation efficiency of on-chip antennas are severely affected by substrate loss, slots and thin dielectric layers⁶. In addition, surface waves that are induced on the antenna can distort the radiation pattern in terms of beamwidth as well as degrade its gain⁷. A simple technique in⁸ redirects the radiated signal back to the front-side by using a reflective surface under the silicon substrate on which the antenna is implemented. This technique is viable for broadside radiation antennas. However, the drawback of this technique is that it makes the antenna gain highly sensitive to the on-chip circuit vias and metal routings. To date, various other techniques have been explored to improve the performance of on-chip antennas, including the use of thinner substrates⁷, artificial magnetic conductors⁹, micromachining¹⁰, silicon lenses¹¹, and dielectric resonators (DR)¹². However, these techniques compromise the antenna gain performance and add complexity to their fabrication. In addition, DR antennas leak electromagnetic (EM) energy into the lossy CMOS silicon substrate, which degrades the antenna efficiency.

This paper presents a novel antenna design that exhibits a high gain and high efficiency over a wide operating bandwidth, while at the same time its miniature size makes it suitable for off-chip THz applications such as anti-counterfeiting security tags and quantum sensors¹³. The unique feature of the proposed antenna is a meandering transmission line structure which is loaded with multiple slots over its length and the line is terminated with metamaterial-inspired impedance matching circuit (MTM-IMC). The size and periodicity of the slots is subwavelength over the frequency band of operation. These characteristics transform the meandering line to a metasurface^{14,15}. The proposed antenna is implemented on a multilayer stack of 400 μm thick silicon substrate ($\epsilon_r = 11.9$). The antenna is excited with an open-circuited microstrip line by coupling RF energy through a slot, which is implemented on a ground-plane sandwiched between two silicon layers. Such a THz antenna can provide high spatial resolution that overcomes the limitation of for example RFID tags in their ability to resolve other RFID devices in close proximity¹⁶.

Off-chip antenna design

Metamaterials (MTM) exhibit a negative refractive index, and a metamaterial unit cell can be modelled using an equivalent electrical T-circuit comprising series capacitors and a shunt inductor¹⁷. The negative refractive index exhibited by the metamaterial is due to the resonance of the unit cell, which makes the metamaterials inherently dispersive. The electromagnetic properties of such materials are highly sensitive to the changes in the operating frequency, which makes them bandwidth limited. Metasurfaces are two-dimensional or surface counterparts of metamaterials. Metasurfaces can be implemented using an array of subwavelength resonant scatters consisting of dielectric slots constructed on a transmission line^{14,15}. The size and periodicity of the individual slots need to be small in comparison to the wavelength of operation, which is different from frequency selective surfaces (FSS) where individual elements are spaced by $\lambda/2$ at the operating wavelength. It has been shown in¹⁸ that the dispersion characteristics of metasurfaces are broadened with multiple scatterers. This principle is applied in the proposed antenna design.

The proposed off-chip antenna (OCA) is constructed on a stack of three silicon layers. The antenna is realized on the surface of the top layer. The bottom side of the top silicon layer is a ground-plane on which a narrow slot line is created. On the bottom side of the second silicon layer is a feed structure consisting of an open-circuited microstrip line which is aligned with the slot line and the input port to the antenna. Stacked over the feedline is a substrate layer whose outward facing side is ground-plane to shield the OCA from being susceptible to materials on which it is mounted on. The radiating element of the OCA is an elongated and folded open-circuited loop transmission line whose other end is terminated with a metamaterial-inspired impedance matching circuit, as shown in Fig. 1. Although by meandering the antenna some discontinuity is created however this was necessary to reduce its footprint. The meandering antenna is loaded with a series of regularly spaced circular dielectric slots along its length. The size and periodicity of the individual slots is smaller than the wavelength of operation. The slots act like subwavelength resonant scatters that transforming the meandered line into a metasurface^{14,15}. The antenna is excited from underneath by coupling RF energy from the open-circuited feedline through the rectangular slot implemented on the middle ground-plane layer.

Unlike standing wave antennas, the circular slots implemented on the meandering line antenna do not need to be excited in-phase. Consequently, the gap between the slots do not depend on the wavelength of the signal. It will be shown later that this results in a structure that exhibits a higher impedance bandwidth compared to the standing wave structure.

The MTM-IMC is a cross-shaped microstrip structure with slots, as shown in Fig. 1. It is capacitively coupled to the antenna and is grounded with metallized via-holes. This structure is a left-handed metamaterial whose equivalent electrical circuit consists of a series left-handed capacitance (C_l) and shunt left-handed inductance

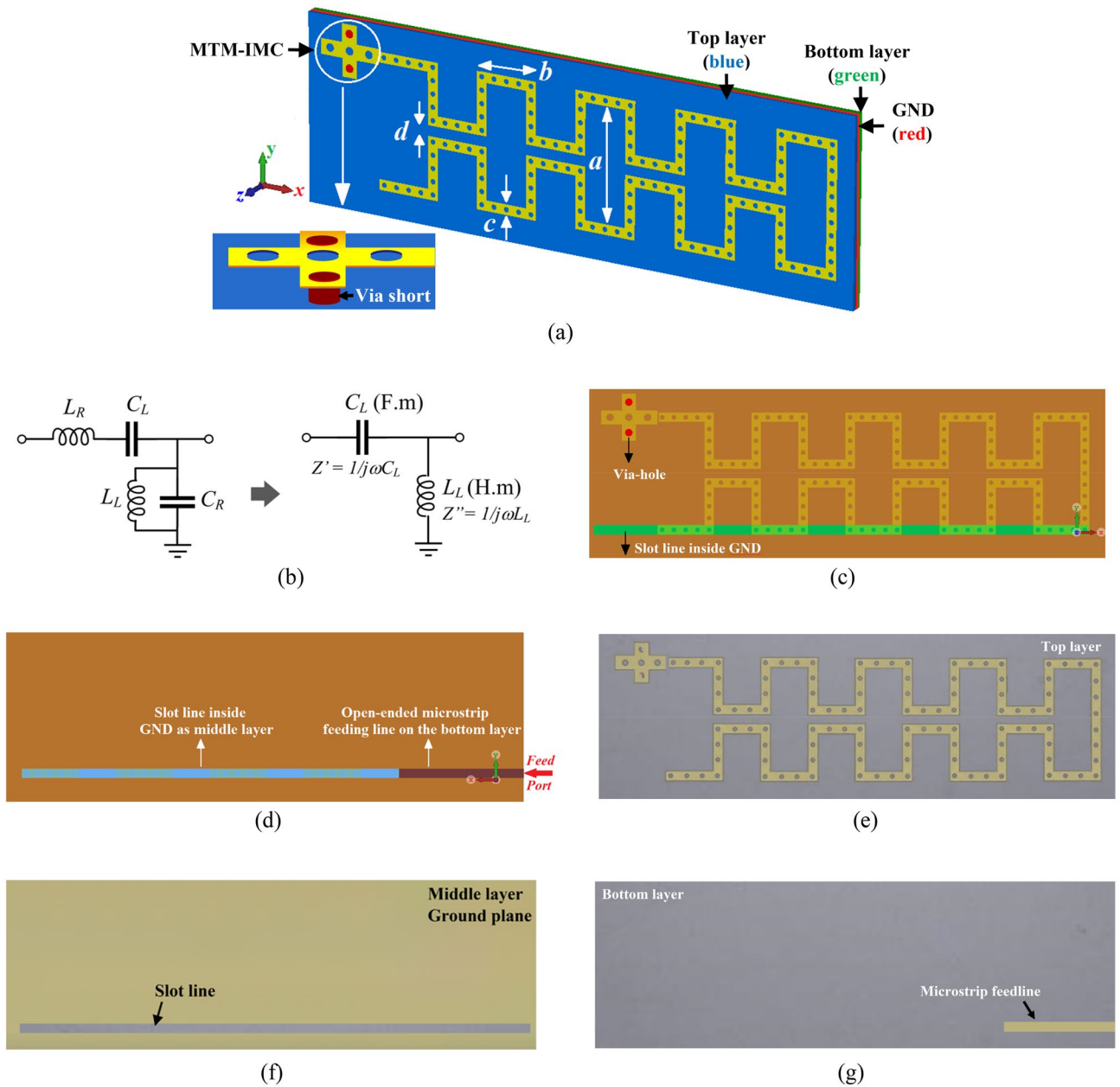


Figure 1. Proposed on-chip antenna, (a) simulated isometric view of the OCA structure showing a close-up view of the MTM-IMC, (b) equivalent circuit model of the MTM-IMC, (c) top-view of the antenna layout along with an overview of the coupling slot line on the ground plane showing its precise location underneath the slotted meandering line, (d) back-side of the simulated layout with an overview of the coupling slot line on the ground plane showing its precise position in relation to the open-ended microstrip feedline, (e) top-view of the fabricated prototype OCA, (f) fabricated middle ground-plane layer (GND) with coupling slot line, and (g) fabricated back-side of the OCA showing the open-ended microstrip feedline, which is shielded with a substrate layer whose outward face side is a ground-plane.

(L_L)¹⁷. The MTM-IMC structure has unavoidable fringing fields resulting from the currents flowing on the surface of the antenna and the gap between the surface and the ground-plane. Hence, the fringing fields create right-handed parasitic elements of series right-handed inductances (L_R) and shunt right-handed capacitances (C_R) associated with the left-handed components. The equivalent circuit of the MTM-IMC is shown in Fig. 1b. The magnitude of the reactive components resulting from the fringing fields are negligible and can be therefore ignored in the analysis. The equivalent circuit then simplifies to series C_L and shunt L_L . For simplicity, assuming loss-less case, the propagation constant γ , the propagation constant β , the phase velocity v_p , and the group velocity v_g of the transmission-line can be shown to be given by

$$\gamma = j\beta = \sqrt{Z'Y''} = -j1/\omega\sqrt{L_L C_L} \tag{1}$$

Thickness of silicon substrate	400
Thickness of metalized ground-plane layer	35
Thickness of microstrip conductor	35
Radius of circular MTM-IMC slots	85
Gap between the MTM-IMC slots	340
Radius of meander line slots	45
Gap between the meander line slots	300
Radius of metallic via-holes	85
Gap between the via-holes and slots	330
Length of the ground-plane slot	11,900
Width of the ground-plane slot	380
Length of the microstrip feedline	3500
Width of the microstrip feedline	380
Parameter <i>a</i> in Fig. 1a	2677
Parameter <i>b</i> in Fig. 1a	1151
Parameter <i>c</i> in Fig. 1a	380
Parameter <i>d</i> in Fig. 1a	375

Table 1. Structural dimensions of OCA (unit : μm).

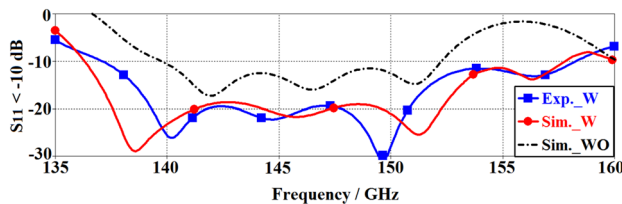


Figure 2. Simulated and measured reflection-coefficient response of the proposed OCA without (WO) and with (W) the MTM-IMC termination and slots.

$$\beta = -1/\omega\sqrt{L_L C_L} \quad (2)$$

$$v_p = \omega/\beta = -\omega^2\sqrt{L_L C_L} < 0 \quad (3)$$

$$v_g = (\partial\beta/\partial\omega)^{-1} = +\omega^2\sqrt{L_L C_L} > 0 \quad (4)$$

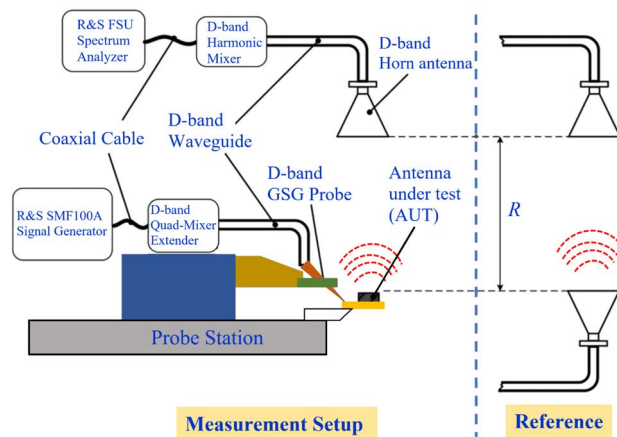
Eqs. (3) and (4) show that the phase velocity, associated with the direction of phase propagation, is negative, whereas the group velocity, associated with the direction of power flow, is positive. These characteristics are manifestation of metamaterials. The geometrical parameters of the proposed OCA are listed in Table 1. Its overall physical dimension is $12.3 \times 4.5 \times 0.905 \text{ mm}^3$.

Measured results

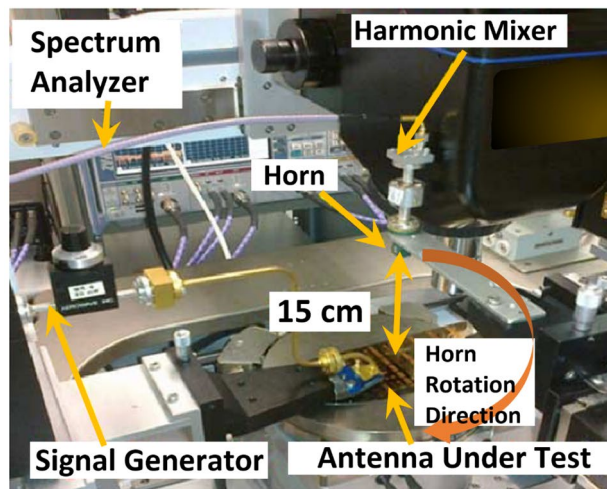
The simulated and measured reflection-coefficient response of the proposed OCA are compared in Fig. 2 with and without the MTM-IMC and slots. The simulation was done with the 3D full-wave EM tool CST Microwave Studio.

The simulation results in Fig. 2 show that without MTM-IMC plus slots, the antenna's impedance bandwidth for $S_{11} < -10 \text{ dB}$ is 0.012 THz (0.14–0.152 THz), which corresponds to a fractional bandwidth of 8.21%. With MTM-IMC plus slots the measured impedance bandwidth is significantly improved by a factor of approximately 2–0.021 THz (0.137–0.158 THz), which corresponds to a fractional bandwidth of 14.23%. Moreover, across 0.14–0.152 THz range, the average impedance matching with MTM-IMC plus slots is better than -21 dB , whereas without MTM-IMC plus slots it is limited to -13 dB . The empirical results clearly demonstrate a significant improvement in the reflection coefficient by 8 dB, and this is an indication of its effectiveness in suppressing losses attributed to surface waves and substrate losses. Figure 2 also shows very good agreement between the simulated and measured results.

In addition to the impedance bandwidth, the other characteristics that define the antenna's performance are the gain and radiation efficiency. The measurement of these parameters for the OCA required a probe station setup as described in¹⁹, which is illustrated in Fig. 3a. The photograph of the setup used is shown in Fig. 3b. The signal from the R&S SMF 100A was applied to a D-band quad-mixer extender. The transmission signal from the



(a)



(b)

Figure 3. (a) Diagram of the on-wafer measurement setup for the power gain test. (b) Photograph of the on-wafer gain measurement setup.

mixer is fed to the OCA using a D-band waveguide-to-GSG probe. The received signal at the D-band standard horn antenna is down-converted through a harmonic mixer and fed to the R&S SMF Spectrum Analyzer for measurement. The horn antenna was used to sense the radiation from the OCA at a far-field distance of 15 cm. The OCA was then replaced by another standard horn antenna, and the antenna gain was obtained using the traditional method of comparing the power received by the standard horn of a known gain with that received by the OCA. Measurements done consider the waveguide-to-GSG probe loss of ~ 1.6 dB and the waveguide-to-horn transition loss of ~ 1 dB.

The directivity/gain method was used to measure the radiation efficiency using the expression $\eta = G/D$, where G is the gain of the OCA measured using a standard gain horn, and D is the directivity of OCA. Directivity was determined from the expression $D = 41,253/(\Delta\theta\Delta\phi)$, where $\Delta\theta$ and $\Delta\phi$ are the principal plane beamwidths (in decimal degrees) measured from the radiation pattern of the antenna²⁰. The equipment other than the OCA and horn antenna was covered with radiation absorbent material (RAM) to prevent the reflections from affecting the measurements. The OCA's back lobe was measured by rotating the horn antenna under the OCA, but this was limited due to the measurement setup used. Figure 4a shows the simulated gain of the OCA including MTM-IMC under two scenarios, with slots and without slots. It is evident that with the slots there is a gain improvement of about 3 dB. The measured gain and radiation efficiency of the OCA before and after applying MTM-IMC and slots are shown in Fig. 4b,c, respectively. These results show good agreement between the simulation and measurement. The average gain and efficiency prior to implementing the proposed MTM-IMC plus slot is 4 dBi and 46%, respectively. After applying the MTM-IMC plus slot, the measured gain and efficiency significantly increase to 8.6 dBi and 77%, respectively. This constitutes an improvement of 4.6 dBi and 31% in the gain and the efficiency, respectively. These results are summarized in Table 2.

The simulated radiation patterns of the proposed OCA with the MTM-IMC termination at two spot frequencies in its operating band are shown in Fig. 5. This antenna radiates in the broadside over its entire length. The simulated and measured radiation patterns in the two orthogonal planes are shown in Fig. 6. The radiation coverage in the $E(x-z)$ -plane is 180° along the length of the antenna. However, the $H(y-z)$ -plane radiation pattern

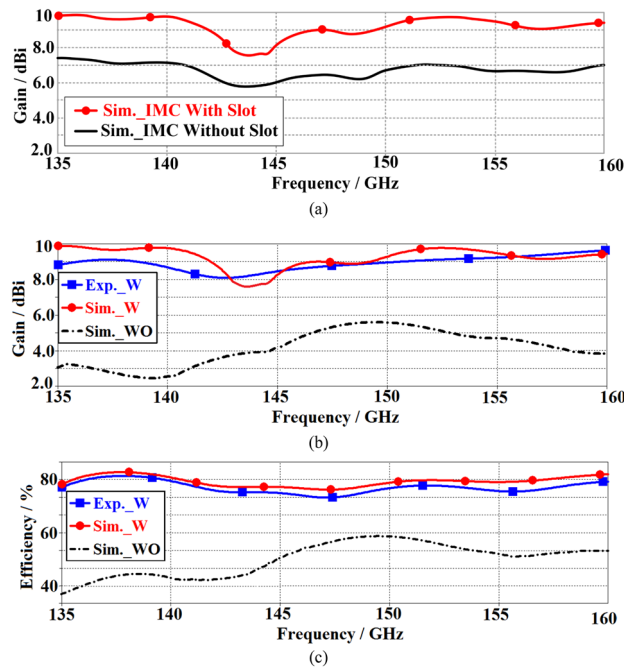


Figure 4. (a) Simulated gain of the OCA under two conditions, (1) MTM-IMC and without (WO) slot, and (2) MTM-IMC and with (W) slots, (b) simulated and measured gain of the OCA before and after applying MTM-IMC and slots, and (c) simulated and measured efficiency of the OCA before and after applying MTM-IMC and slots radiation efficiency.

	Gain (dBi)	Efficiency (%)
Without MTM-IMC plus slots (simulated)		
Maximum	5.6 @ 149 GHz	59 @ 150 GHz
Minimum	2.5 @ 140 GHz	37.5 @ 135 GHz
Average	4	46
With MTM-IMC plus slots (measured)		
Maximum	9.6 @ 158 GHz	81 @ 137.5 GHz
Minimum	8.1 @ 143 GHz	74 @ 147.5 GHz
Average	8.6	77
Improvement with MTM-IMC plus slots		
Average	4.6	31

Table 2. Radiation characteristics.

is attenuated at its sides. These results show that changes in frequency does not cause significant changes in the radiation patterns. Also, there is good correlation between the simulated and measured results.

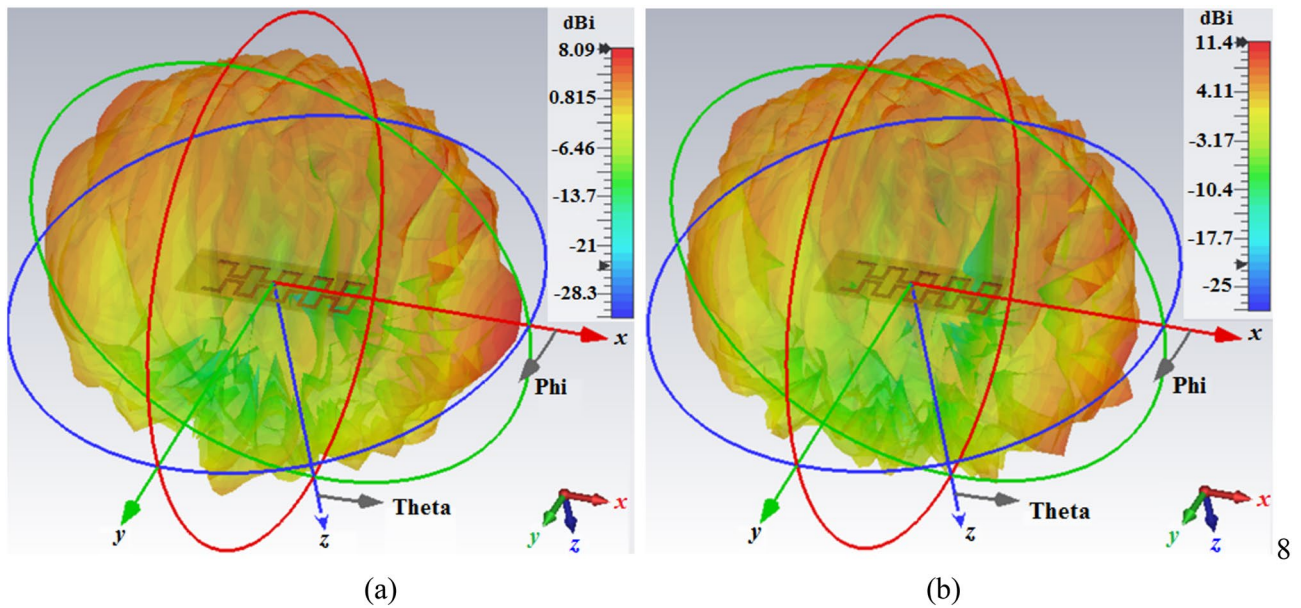


Figure 5. Radiation patterns of the proposed OCA with the MTM-IMC termination and slots at (a) 0.137 THz, and (b) 0.158 THz.

The radar cross section (RCS) of OCA that characterizes its backscattering was measured. The measured RCS for the proposed OCA, in Fig. 7, was calculated using the expression $RCS = |S_{11}|^2 [(4\pi)^3 r^4 / (\lambda G)^2]$, where S_{11} is the magnitude of the reflection coefficient at wavelength λ , G is the gain of the transmitting antenna, and r is the distance to the tag antenna^{21,22}. RCS is better than -23 dBm² from 135 to 160 GHz.

Comparison with prior research

In this section, the performance of the proposed OCA is compared with other antennas that can be integrated in sub-THz and THz wireless systems. The comparison shown in Table 3 confirms that the proposed antenna structure having a fractional bandwidth of 14.23% supports a wider operational bandwidth than other antennas except for references^{23–26}. Moreover, the proposed OCA has the highest average gain and efficiency performances. Although the dimensions of the proposed antenna are bigger than other cited works, its structure is less complex to implement in practice, and therefore it is more cost effective. These characteristics make the antenna viable for sub-THz integrated RFID circuits for wireless applications. The present work was a feasibility study. However, in the future we intend to reduce the antenna size by decreasing the gap between the folds of the meandering line, and by using a substrate with a higher permittivity.

Conclusion

The proposed meandering line THz antenna structure is shown to exhibit high gain and high efficiency performance. The antenna structure was fabricated on a stack of three silicon layers and consists of a single meandering line that is loaded with a series of regularly spaced circular slots along its length and terminated by a metamaterial-based impedance matching circuit. The antenna radiates power through the circular slots when it is excited using an open-ended microstrip line realized on the bottom silicon layer. Electromagnetic energy is coupled from the feedline to the top silicon layer through a slot line etched in the middle ground-plane layer. The measurements confirm that the fabricated antenna has a relatively large fractional bandwidth of 14.23%, a peak gain of 9.6 dBi and the maximum radiation efficiency of 81%. Such characteristics of wide bandwidth, high gain, and high efficiency makes the antenna an excellent candidate for integrating with sub-terahertz near-field electronic systems.

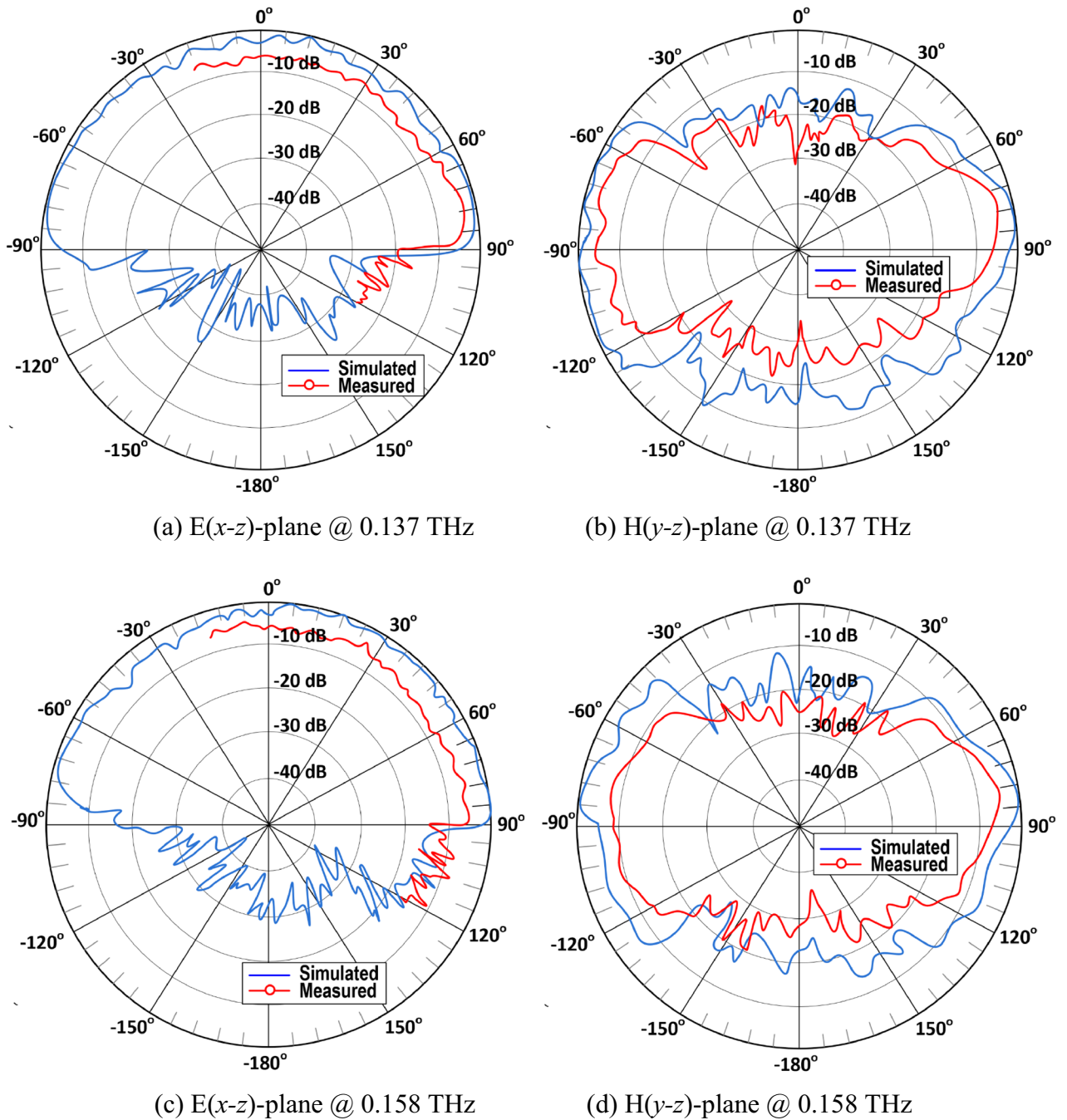


Figure 6. Normalized simulated and measured radiation patterns in the E-plane and H-plane of the proposed OCA with the MTM-IMC termination and slots.

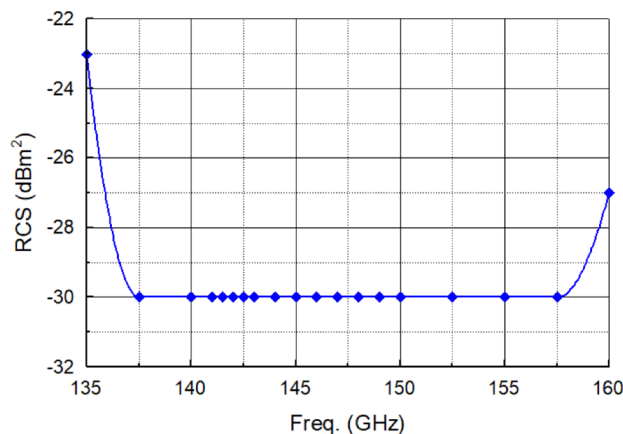


Figure 7. Measured radar cross section (RCS) of the proposed OCA tag.

References	Type	FBW (%) / [Freq. range (GHz)]	Ave. Gain (dBi)	Max. Gain (dBi)	Eff. (%)	Size (mm ³)	Complexity
²³	Bowtie-slot	15.38/[90–105]	−2.2	−1.78 @ 98 GHz	–	0.71 × 0.31 × 0.65	High
²⁴	Circular open-loop	16.13/[57–67]	−5.0	−4.4 @ 66 GHz	–	1.8 × 1.8 × 0.3	High
²⁷	Dipole-antenna	7.1/[95–102]	–	4.0 @ 94 GHz	–	–	Moderate
²⁸	Cavity fed DRA	11.32/[125–140]	4.0	7.5 @ 133 GHz	Max. 42	0.8 × 0.9 × 2.2	High
¹⁹	Slot fed DRA	7.7/[125–135]	2.0	4.7 @ 125 GHz	Max. 43	0.9 × 0.8 × 1.5	High
²⁵	DRA	15.38/[120–140]	−2.0	4.1 @ 125 GHz	Max. 43	0.9 × 0.8 × 0.6	High
²⁹	4 × 1 Patch array	11.63/[259–291]	–	11.2 @ 275 GHz	–	2.47 × 1.53 × 0.67	Moderate
³⁰	2 × 1 Shorted annular ring	5.45/[303–320]	1.0	5.0 @ 315 GHz	Max. 38	0.55 × 1 × 0.13	High
²⁶	Dipole loaded AMC	33.67/[200–281]	0	2.0 @ 96 GHz	Max. 63	0.25 × 0.41 × 0.13	Moderate
³¹	2 × 2 slot array	2.74/[323–332]	3.0	7.9 @ 320 GHz	–	0.86 × 0.86 × 0.13	High
³²	2 × 2 DRA array	2.34/[334–350]	1.0	8.65 @ 338 GHz	54	2.2 × 1.4 × 0.65	High
This work	OCA with MTM-IMC	14.23/[137–158]	8.6	9.6 @ 158 GHz	Max. 81 @ 137.5 GHz	12.3 × 4.5 × 0.905	Low

Table 3. Performance comparison.

Data availability

All data generated or analysed during this study are included in this article.

Received: 5 April 2022; Accepted: 19 October 2022

Published online: 25 October 2022

References

- Huang, S.-X. *et al.* Terahertz Mueller matrix polarimetry and polar decomposition. *IEEE Trans. THz Sci. Technol.* **10**(1), 74–84 (2020).
- Cheng, L. *et al.* Research of nondestructive methods to test defects hidden within composite insulators based on THz time-domain spectroscopy technology. *T-DEI* **23**(4), 2126–2133 (2016).
- Tokgoz, K. K. *et al.* A 120 Gb/s 16QAM CMOS millimeter-wave wireless transceiver. In *IEEE International Solid-State Circuits Conference* 168–170 (2018).
- <http://www.teraview.com/products/TeraPulse%204000/index.html>.
- Zhong, J.-Y. *et al.* A high spectral efficiency receiver at 57–66 GHz using 65-nm CMOS in LTCC package with polarization MIMO. *IEEE Access* **7**, 129466–129479 (2019).
- Han, R. *et al.* A 280-GHz Schottky diode detector in 130-nm digital CMOS. *IEEE J. Solid-State Circuits* **46**(11), 564–580 (2011).
- Sengupta, K. & Hajimiri, A. A 0.28 THz power-generation and beamsteering array in CMOS based on distributed active radiators. *IEEE J. Solid-State Circuits* **47**(12), 3013–3031 (2012).
- Jameson, S. *et al.* A 300 GHz wirelessly locked 2 × 3 array radiating 5.4 dBm with 5.1% DC-to-RF efficiency in 65 nm CMOS. In *Proceedings of IEEE International Solid-State Circuits Conference on Technical Digest* 348–349 (2016).
- Bao, X.-Y., Guo, Y.-X. & Xiong, Y.-Z. 60-GHz AMC-based circularly polarized on-chip antenna using standard 0.18-μm CMOS technology. *IEEE Trans. Antennas Propag.* **60**(5), 2234–2241 (2012).
- Ojefors, E., Kratz, H., Grenier, K., Plana, R. & Rydberg, A. Micromachined loop antennas on low resistivity silicon substrates. *IEEE Trans. Antennas Propag.* **54**(12), 3593–3601 (2006).

11. Grzyb, J., Zhao, Y. & Pfeiffer, U. R. A 288-GHz lens-integrated balanced triple-push source in a 65-nm CMOS technology. *IEEE J. Solid-State Circuits* **48**(7), 1751–1761 (2013).
12. Buadana, N., Jameson, S. & Socher, E. A multiport chip-scale dielectric resonator antenna for CMOS THz transmitters. *IEEE Trans. Microw. Theory Techn.* **68**(9), 3621–3632 (2020).
13. Bunruangsang, M. *et al.* Realizing THz RFID using silicon chip space-time control circuit. *SILICON* **13**(2021), 3621–3632 (2020).
14. Bukhari, S. S., Vardaxoglou, J. & Whittow, W. A metasurfaces review: Definitions and applications. *Appl. Sci.* **9**(2727), 1–14 (2019).
15. Colquitta, D. J. *et al.* Seismic metasurfaces: Sub-wavelength resonators and Rayleigh wave interaction. *J. Mech. Phys. Solids* **99**, 379–393 (2017).
16. Mitsuhashi, R. *et al.* Terahertz tag identifiable through shielding materials using machine learning. *Opt. Express* **28**(3), 3517–3527 (2020).
17. Caloz, C. & Itoh, T. Characteristics of the composite right/left-handed transmission lines. *IEEE Microw. Wirel. Compon. Lett.* **14**(2), 68–70 (2004).
18. Konstantinidis, K. *et al.* Broadband sub-wavelength profile high-gain antennas based on multi-layer metasurfaces. *IEEE Trans. Antennas Propag.* **63**(1), 423–427 (2015).
19. Hou, D. *et al.* 130-GHz on-chip meander slot antennas with stacked dielectric resonators in standard CMOS technology. *IEEE Trans. Antennas Propag.* **60**(9), 4102–4109 (2012).
20. González, J. M. & Romeu, J. Measurement of radiation efficiency and quality factor of fractal antennas: the Wheeler Cap method. In *FRACTALCOMS Report 1–25* (2002).
21. Nikitin, P. V. & Rao, K. V. S. Theory and measurement of backscattering from RFID tags. *IEEE Antennas Propag. Mag.* **48**(6), 212–218 (2006).
22. Grace, M. I. Measurement of radar cross section using the “VNA Master” handheld VNA, Anritsu application note. <https://dl.cdn-anritsu.com/en-us/test-measurement/files/Application-Notes/Application-Note/11410-00604B.pdf>.
23. Khan, M. S., Tahir, F. A. & Cheema, H. M. Design of bowtie-slot on-chip antenna backed with E-shaped FSS at 94 GHz. In *10th European Conference on Antennas and Propagation (EuCAP) 1–3* (Davos, 2016).
24. Bao, X., Guo, Y. & Xiong, Y. 60-GHz AMC-based circularly polarized on-chip antenna using standard 0.18- μ m CMOS Technology. *IEEE Trans. Antennas Propag.* **60**(5), 2234–2241 (2012).
25. Hou, D. *et al.* Silicon based on-chip antenna design for millimeter-wave/THz applications. In *Electrical Design of Advanced Packaging and Systems Symposium 1–4* (2011).
26. Nafe, M., Syed, A. & Shamim, A. Gain-enhanced on-chip folded dipole antenna utilizing artificial magnetic conductor at 94 GHz. *IEEE Antennas Wirel. Propag. Lett.* **16**, 2844–2847 (2017).
27. Nafe, M., Syed, A. & Shamim, A. Gain enhancement of low profile on-chip dipole antenna via artificial magnetic conductor at 94 GHz. In *9th European Conference on Antennas & Propagation (EuCAP) 1–3* (Lisbon, 2015).
28. Hou, D. *et al.* D-band on-chip higher-order-mode dielectric-resonator antennas fed by half-mode cavity in CMOS technology. *IEEE Antennas Propag. Mag.* **56**(3), 80–89 (2014).
29. Benakaprasad, B., Eblabla, A., Li, X., Thayne, I., Wallis, D. J., Guiney, I., Humphreys, C. & Elgaid, K. Terahertz monolithic integrated circuits (TMICs) array antenna technology on GaN-on-low resistivity silicon substrates. In *41st International Conference on Infrared, Millimeter, and Terahertz waves 1–2* (2016).
30. Zhu, H., Li, X., Qi, Z. & Xiao, J. A 320 GHz octagonal shorted annular ring on-chip antenna array. *IEEE Access* **8**, 84282–84289 (2020).
31. Hou, Z. J. *et al.* A 320 GHz on-chip slot antenna array using CBCPW feeding network in 0.13- μ m SiGe technology. In *IEEE MTT-S International Microwave Symposium Digest 843–846* (2017).
32. Li, C.-H. & Chiu, T.-Y. Single flip-chip packaged dielectric resonator antenna for CMOS terahertz antenna array gain enhancement. *IEEE Access* **7**, 7737–7746 (2019).

Acknowledgements

Dr. Mohammad Alibakhshikenari acknowledges support from the CONEX-Plus programme funded by Universidad Carlos III de Madrid and the European Union’s Horizon 2020 research and innovation programme under the Marie Skłodowska-Curie grant agreement No. 801538. Additionally, this work was partially supported by RTI2018-095499-B-C31, Funded by Ministerio de Ciencia, Innovación y Universidades, Gobierno de España (MCIU/AEI/FEDER,UE), and by the Icelandic Centre for Research (RANNIS) Grant 206606, and by National Science Centre of Poland Grant 2018/31/B/ST7/02369.

Author contributions

Conceptualization, M.A., B.S.V., D.M., V.V., M.N.-M., C.H.S., I.D., S.A., P.L., S.N.B., A.P.-D., F.F., S.K., and E.L.; methodology, M.A., B.S.V., D.M., V.V., M.N.-M., C.H.S., I.D., S.A., P.L., S.N.B., A.P.-D., F.F., S.K., and E.L.; software, M.A., B.S.V., D.M., and V.V.; validation, M.A., B.S.V., D.M., V.V., M.N.-M., C.H.S., I.D., S.A., P.L., S.N.B., A.P.-D., F.F., S.K., and E.L.; formal analysis, M.A., B.S.V., D.M., V.V., C.H.S., I.D., S.A., P.L., F.F., and E.L.; investigation, M.A., B.S.V., D.M., V.V., M.N.-M., C.H.S., P.L., S.N.B., A.P.-D., F.F., and S.K.; resources, M.A., B.S.V., D.M., V.V., M.N.-M., C.H.S., I.D., S.A., S.N.B., A.P.-D., F.F., S.K., and E.L.; data curation, M.A., B.S.V., D.M., V.V., M.N.-M., C.H.S., I.D., S.A., S.N.B., A.P.-D., F.F., S.K., and E.L.; writing—original draft preparation, M.A.; writing—review and editing, M.A., B.S.V., D.M., V.V., M.N.-M., C.H.S., I.D., S.A., P.L., S.N.B., A.P.-D., F.F., S.K., and E.L.; visualization, M.A., B.S.V., V.V., C.H.S., I.D., S.A., P.L., S.N.B., F.F., S.K., and E.L.; supervision, M.A., B.S.V., F.F., S.K., and E.L.; project administration, M.A., B.S.V., C.H.S., S.A., F.F., S.K., and E.L.; funding acquisition, M.A., A.P.-D., F.F., S.K., and E.L.

Competing interests

The authors declare no competing interests.

Additional information

Correspondence and requests for materials should be addressed to M.A.

Reprints and permissions information is available at www.nature.com/reprints.

Publisher’s note Springer Nature remains neutral with regard to jurisdictional claims in published maps and institutional affiliations.



Open Access This article is licensed under a Creative Commons Attribution 4.0 International License, which permits use, sharing, adaptation, distribution and reproduction in any medium or format, as long as you give appropriate credit to the original author(s) and the source, provide a link to the Creative Commons licence, and indicate if changes were made. The images or other third party material in this article are included in the article's Creative Commons licence, unless indicated otherwise in a credit line to the material. If material is not included in the article's Creative Commons licence and your intended use is not permitted by statutory regulation or exceeds the permitted use, you will need to obtain permission directly from the copyright holder. To view a copy of this licence, visit <http://creativecommons.org/licenses/by/4.0/>.

© The Author(s) 2022